An Air Sampler for Mobile Platforms Measuring Mixing Ratios via Diode and Quantum Cascade Lasers.

Rex J. Fleming

Global Aerospace, LLC

Revised December 26, 2007

1. Introduction

There is an emerging paradigm for the use of commercial aircraft and unmanned aerial vehicles (UAVs) for various measurements: atmospheric water vapor mixing ratios for use in aviation weather; the use of such mixing ratios for weather and climate in general; and the determination of mixing ratios of atmospheric trace gases for use in air quality and climate change. In these applications, the mixing ratios of the quantities to be measured are conserved properties whether determined in static conditions or in fully dynamic conditions. This paper describe the use of a new mobile air sampler that makes maximum use of the diode laser and quantum cascade (QC) lasers that have become available.

Commercial jet aircraft have typically used an air sampler for temperature called a total air temperature (TAT) probe that measures the total (dynamic) air temperature and from which the static (ambient) air temperature can be obtained. The mathematical relationship between dynamic temperature and static temperature due to the Mach number (speed of the aircraft relative to the speed of sound) effect is given as the first equation in the Appendix. Similar expressions for dynamic pressure and dynamic density are also found there. This TAT probe extends from the aircraft about three inches away from the friction-heated layer of air next to the aircraft's metal surface.

The TAT probe includes a probe heater, which is the source of its highest failure mode. The probe also suffers from a friction drag that is an effective 2.5 lbs, which increases an already significant fuel bill for the aviation industry. The TAT also has a radar cross section that makes it non-stealthy – a concern in some military applications.

This article describes a new mobile air sampler that is perfectly matched to this new paradigm. The new UCAR air sampler **(United States Patent Number 6,809,648)** has been designed with three goals in mind. The first goal is to utilize the conservative properties of mixing ratios and avoid the negative features of the extended air samplers on aircraft. The second and third goals are related to a diversion of the airflow in the sampler – one part of the flow is speeded up to remove unwanted atmospheric constituents and a second part of the flow is slowed down to optimal conditions for the measurement cell. It is the measurement cell technology – frequency modulation spectroscopy using single mode diode lasers and quantum cascade (QC) lasers – that will make maximum use of the air sampler. A deeper explanation of the air sampler design and its use with the above technologies will be revealed in the following sections.

Section 2 will describe the first intended use of the air sampler in an off-the-shelf product for commercial aircraft measuring atmospheric water vapor mixing ratios. This application will serve to introduce the three design goals for the air sampler. Section 3 provides a theoretical basis for certain design features and dimensions of the air sampler. Section 4 describes simulation results that use both incompressible and compressible flow theory to help justify the design features. Section 5 comments on the efficiency of ice crystal, liquid water droplets, and aerosol removal.

Section 6 will conclude the paper with a description of the broad intended use of the air sampler in the weather and climate community for both more accurate water vapor measurements and for profiles of atmospheric trace gases.

2. Water Vapor Mixing Ratio Measurements

Accurate water vapor information is required for a spectrum of socio-economic applications in atmospheric science. The literature contains many references to the value of water vapor for weather and climate analysis and prediction. Fleming (1996) discussed its importance in the aviation weather impacts area. Crook (1996) showed the sensitivity of convection to the vertical moisture profile, where inaccuracies in water content lead to large difference in model-predicted rainfall amounts. Lorenc et al (1996) demonstrated the importance of accurate information of water vapor amounts in the determination of fractional cloud cover in forecasts. Bates, et al. (1996) pointed out the value of improved in situ measurements of water vapor to help provide an absolute calibration of satellite data to provide a better climatology of upper-tropospheric water vapor.

Knowledge of water vapor over the four dimensions of space/time is important, but, unfortunately, its spatial and temporal variability far exceeds the current capability of the radiosonde network, e.g.; Melfi, et al. (1989), Miloshevich, et al. (1998). Finally, water vapor is not dynamically constrained like the wind, pressure, and temperature fields (cf. Emanuel, et al., 1995), thus making it more variable and more difficult to measure.

The measurement of relative humidity (RH) via a thin-film capacitor within a commercial aircraft TAT probe was described by Fleming, et al., 2002. This was a proof of concept effort that was successful in that regard, but revealed the limitations of RH sensors on aircraft. A more accurate measurement system for water vapor mixing ratios and one with a considerably longer lifetime is called the Water Vapor Sensing System version II (WVSS-II). This system uses a diode laser to measure accurately the atmospheric water vapor mixing ratio. This was first proven on high altitude balloons

and NASA research aircraft (cf. May, 1998). These first applications were "open path" systems with the laser beam extending through the open air beneath the balloon or aircraft. The measurement concept uses Beer's Law in the form:

$$I = I_o \exp(-\sigma n l) \quad (1)$$

where I = the laser light intensity at detector

I_o = laser initial intensity

σnl = absorbance

with n = number density of absorbing species

l = optical path length

σ = molecular absorption cross section, a function of pressure and temperature near the laser light path

In the usual application of the above formula, I and I_o are measured, σ and l are known, and thus the number density (n) can be calculated from all the other available quantities. For increased detection sensitivity, thus higher precision and accuracy, second harmonic detection is utilized in which a small-amplitude wavelength modulation is added to the laser current (described in May, 1998 and in greater detail in May and Webster, 1993).

The commercial version of the WVSS-II uses a diode laser with a 20-year lifetime. The sensitivity of the laser receiver, the power of the diode laser, and the sensitivity of the 2nd harmonic calculation all contribute to the fact that the laser light can degrade from 100% down to 2% and still good answers can be achieved. Such degradation can occur from actual laser power loss or from "apparent" laser power loss due to a dirty reflector inside the probe or measurement cell. It is this allowable

degradation that suggests that the maintenance period will be 2+ years. The UCAR air sampler also has a 20 year lifetime.

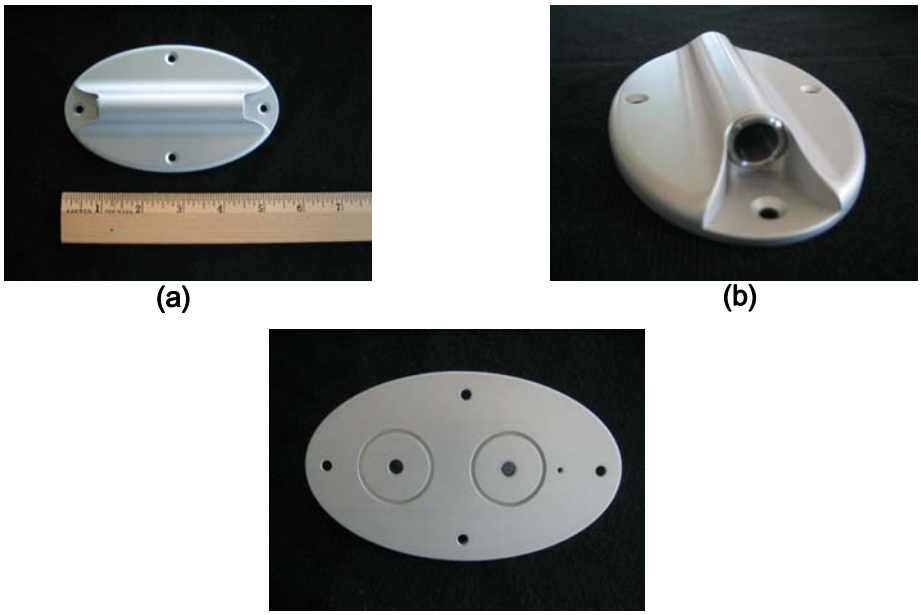

Fig. 1. UCAR air sampler (a) top view, (b) side view, and (c) bottom view.

Fig. 1 shows pictures of the UCAR air sampler from several perspectives. It is only 5.375 inches (13.65 cm) long and flush mounted (virtually no drag) with the aircraft skin. The actual flow through the air sampler is from a region about 0.75 cm to 2.0 cm. from the aircraft so there is no "skin effect". The fact that the aircraft skin friction could provide a small delta in temperature above the ambient air temperature is of no concern to our measurement as the mixing ratio is conserved. **This achieves our first goal of a more efficient aircraft air sampling system.** Whatever the temperature and pressure within the measurement cell may be, it is measured near the laser path so that the molecular absorption cross section term in Eq. (1) is accurate.

The diode laser frequency for water vapor is 1.37 μm. This frequency is not **absorbed** by ice crystals or aerosols; however, a very large number of such ice crystals or

aerosols could **scatter** the laser light and reduce the sensitivity of the diode laser at the cold dry regions of the upper troposphere. This is not an issue for the long path lengths of the "open path" systems, but could be an issue for the shorter path length commercial aircraft system. **Thus, a second goal of the sampler design is to remove ice crystals and aerosols that could hinder the sensitivity of the measurements in the cold, dry upper troposphere.**

An inertial separator is used to remove most of these particles and the NCAR air sampler is aerodynamically designed to do this as described later. Since these particles have a density which ranges from a factor of 10 (new snow) to 100 (snow crystals) to 1000 (aerosols) more dense than the gaseous water vapor, they can be inertially separated by accelerating the flow over the aperture in the air sampler leading to the measurement cell and forcing the majority of such particles out of the rear of the external portion of the air sampler. The degree of efficiency of this process is discussed further in Section 5 but simulations suggest a range from 90 to 97 % of the particle volume present being removed. This particle volume is itself quite small compared to the volume of moist air under normal conditions (Warneck, 1988).

The third goal of the UCAR air sampler design is to slow the flow to the measurement cell inside the aircraft. This is achieved by an obstacle in the air sampler and by the smaller diameter hose feeding air into the larger diameter measurement cell as discussed in the next section.

The amount of flow desired in the measurement cell is a conservative 2-8 meters per second. The response time of the diode laser is fast, but high frequency spectra are averaged to produce a final answer every second. Requiring a minimum of two complete

flushes of air in the cell per unique sample (every second) would demand a flow of 24 cm s^{-1} to flush the cell (12 cm long). Our range is 8-32 times the minimum requirement.

Fig. 2 (lower right) shows the complete WVSS-II system with the hoses that transfer the flow to and from the air sampler to the System Electronics Box (SEB) which houses the measurement cell, laser system, and the electronics. The lower left portion of the figure shows the size of a diode laser relative to a penny.

Fig. 2. Complete WVSS-II commercially available product from SpectraSensors.

The success of the air sampler design, and indeed of Randy May's diode laser system for water vapor, is seen in the NOAA P3 flight results shown in Figs. 3 and 4. Fig. 3 shows the pressure readings of the aircraft on a portion of the flight on July 21, 2004 called a "porpoise" flight where the aircraft flies a series of up and down maneuvers with vapor mixing ratios varying by a factor of 5 (from 25,000 ppmv to 5000 ppmv). Fig. 4 shows that all four water vapor measurement systems (two chilled mirrors, the May "open path" system and the WVSS-II clearly agree extremely well in value. Both of

these laser systems agree with the chilled mirrors except when they "overshoot" in rapidly changing conditions. [Data provided by Richard McNamara of NOAA.]

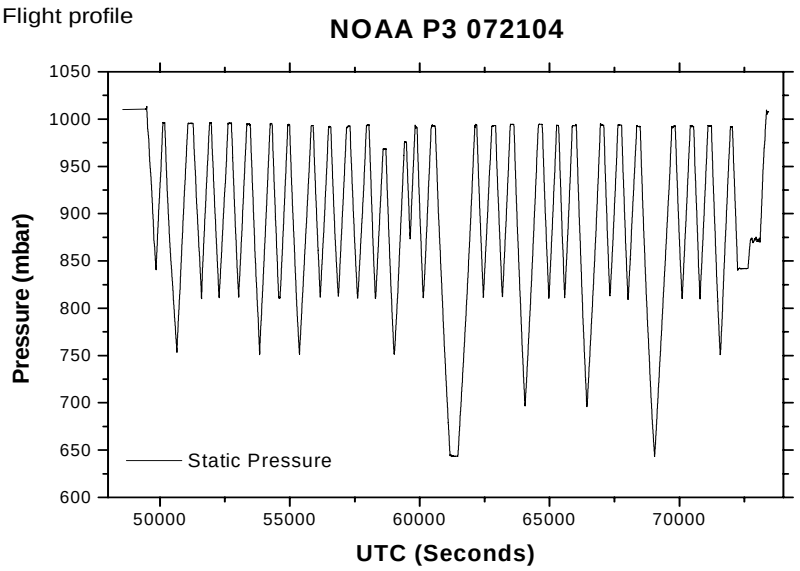

Fig. 3. Pressure record from a portion of a NOAA P-3 flight

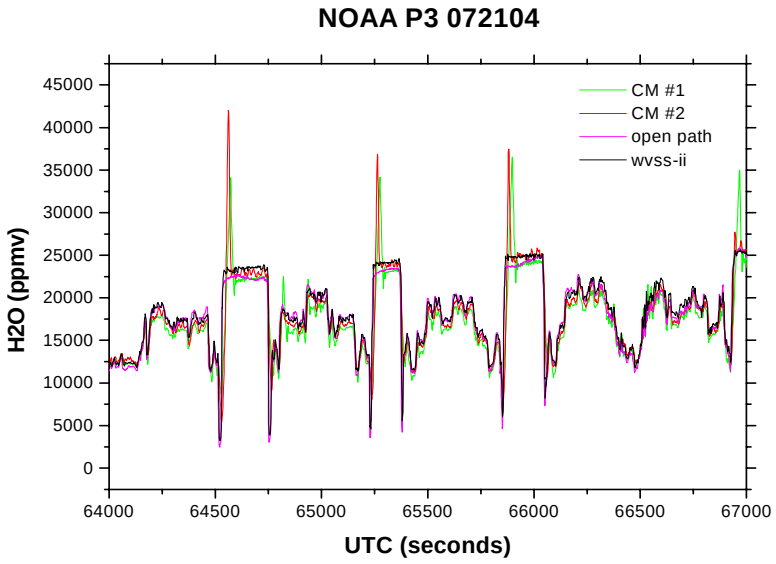

Fig.4. Mixing ratios from two chilled mirrors and two laser systems

Fig. 5 and Fig 6 below show results of the WVSS-II on UPS aircraft taking off from the UPS main operations center in Louisville, KY. Radiosonde data at the same time was provided by an independent party (Wayne Feltz of the U. of Wisconsin). The radiosonde data, 1000 Z (dew points on the left) are reproduced by the WVSS-II, 1021 Z. Fig. 6 shows the consistency of three consecutive aircraft – all matching the radiosonde data.

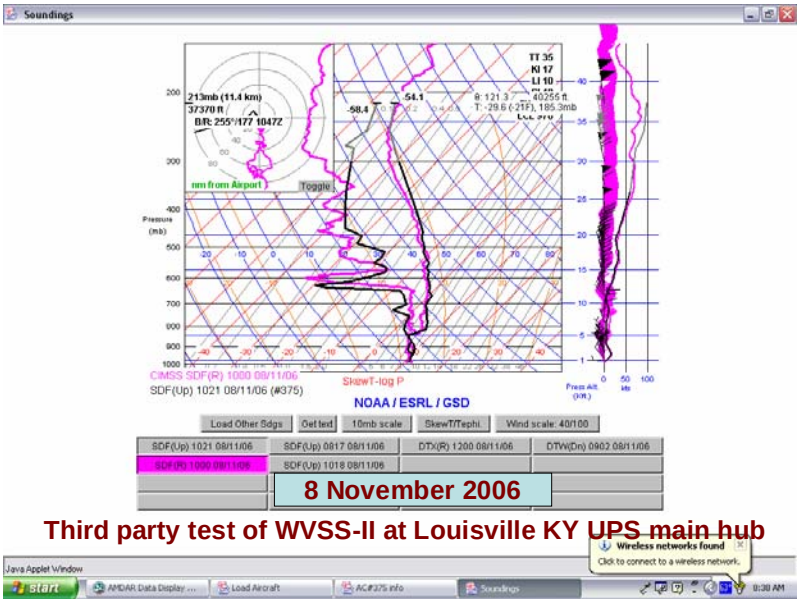

Fig. 5. Radiosonde (pink) and aircraft (black) data at Louisville

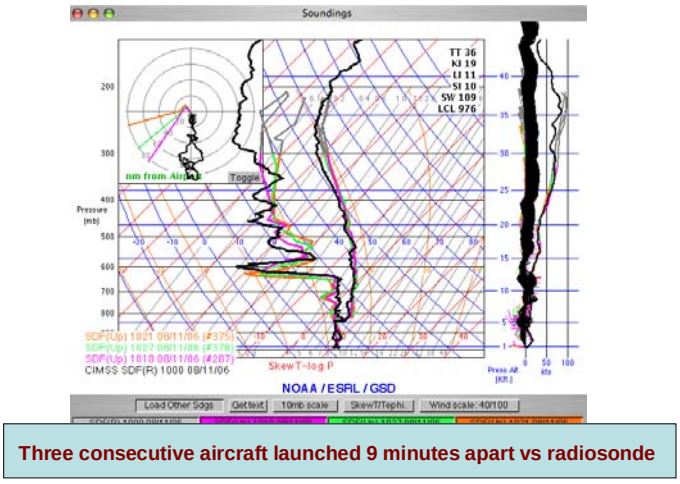

Fig. 6. Three consecutive aircraft (departing at 1018, 1021, and 1027 Z)

3. Example of air sampler in Compressible Quasi-One-Dimensional Theory

The maximum Mach number expected to be encountered by the flush mounted UCAR air sampler is M=0.6 (based upon the position of the sampler on aircraft that typically have a maximum cruise speed of M=0.8 to 0.82). A convergent nozzle design will first accelerate this flow to M=0.72 with an area ratio of $A_{input}/A_{throat} = 1.10$. This is not shown in Fig. 7 (below) but is referred to with the words "Inertial separator (inside)". The analytical result for compressible quasi-one-dimensional flow (e.g., Anderson, 2003) would give a flow velocity at the throat of the sampler (just ahead of the first hose aperture) of 224.4ms^{-1} for a standard atmosphere at 20,000 feet (as shown below).

A useful equation for quasi-one-dimensional flow, which is appropriate for flow through a nozzle, is given by Anderson (2003):

$$\left(\frac{A}{A^*}\right)^2 = \frac{1}{M^2}\left[\frac{2}{\gamma+1}\left(1+\frac{\gamma-1}{2}M^2\right)\right]^{(\gamma+1)/(\gamma-1)} \qquad (2)$$

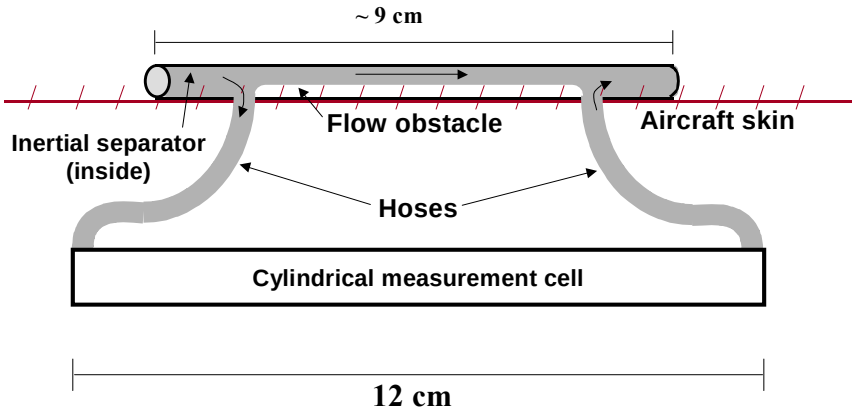

Fig. 7. Cartoon of cross-section of air sampler and measurement cell

Conditions at 20,000 feet for a standard atmosphere, M=0.6, and Eqs. (A1)-(A3) give:

$P = 465.67 \times 10^2$ Pascals $\qquad P_0/P = 1.276$

$\rho = 0.65290$ kg/m^3 $\qquad \rho_0/\rho = 1.190$

$T = 248.5$ K $\qquad T_0/T = 1.072$

and $M = 0.6$ gives $\qquad A/A^* = 1.188$ (from Eq. (2))

Thus, $a = \sqrt{\gamma RT} = 315.99$ ms^{-1} and $U = Ma = 189.6$ ms^{-1}

where P, ρ, T are pressure, density, and temperature; a represents the speed of sound; variables with subscript (0) are "total" variables; and A^* is the area of the throat when M=1. After acceleration through the convergent nozzle, the throat values are:

$$A_T/A^* = \left(A_T/A_I\right)\left(A_I/A^*\right) = \left(1/1.1\right)(1.188) = 1.08$$

which gives $M_{\text{subsonic}} = 0.7206$ (from Eq. (2))

For this $M_T = 0.7206$ one has (the subscript T denotes throat values)

$P_0/P_T = 1.413148$; $\rho_0/\rho_T = 1.280197$; $T_0/T_T = 1.103852$

The new temperature at the throat is calculated in the two-step process:

$T_0 = T_I (T_0 / T) = (248.5) (1.072) = 266.4$ where (T_0 / T) came from input M = 0.60

$T_T = T_0 / (T_0 / T) = 266.4 / (1.1038) = 241.3$ where (T_0 /T) came from throat M = 0.72

Thus, the temperature (and pressure, though not shown) is lower at the throat due to the accelerated flow as compressible flow theory predicts. The new velocity at the throat is:

$$U_T = m_T a_T = m_T \sqrt{\gamma RT_T} = (0.7206)\ (311.4) = 224.4 \text{ ms}^{-1}$$

This throat velocity in the sample cell is the value stated in the introduction to Section 3 above. Our goal is to achieve a **velocity range of 2-8 m/s** in the cylindrical

measurement cell of Fig. 7. This desired flow will be a function of the **flow obstacle** in the sample cell, the diameter of the hoses, and the diameter of the measurement cell (all shown in Fig. 7). The derivation of the desired flow in the measurement cell is shown in the next section.

4. Simulations for the Other Air Sampler Parameters

The UCAR air sampler partitions the flow so that a high velocity flow exits in the rear of the sampler and a slower velocity flow travels through the left hose on its journey to the cylindrical measurement cell. The ratio of "low" flow to "input" flow is a function of sampler geometry, hose aperture size, and the reduced areal flow in the sampler due to the height of the obstacle in the sampler between the hose apertures (see Fig. 7). The high speeds of commercial jet aircraft (Mach number > 0.7 at flight level) require simulations of the air sampler performance with compressible flow theory. This means using the "primitive" equations for such flow. For the lower level ascent/descent conditions where the Mach number is < 0.3 **and for most Unmanned Aerial Vehicles (UAVs)** where M is < 0.3, the flow can be considered to be incompressible and a potential function can be used to relate velocity components. The simulations are described for incompressible flow in Section 4.1 and for compressible flow in Section 4.2.

4.1 Incompressible Flow Theory

Returning to the problem of determining the flow in the hose we note that the quasi-one-dimensional flow assumption used by Anderson (2003) does not apply and one must have a full 2-dimensional nonlinear calculation for the flow. If one assumes incompressible flow, one can solve this problem via the theory of irrotational flow. Here

a potential function Φ is defined such that the x and y components of velocity (U, V) are defined as $\mathbf{U = - \partial \Phi / \partial y}$ $\mathbf{V = \partial \Phi / \partial x}$

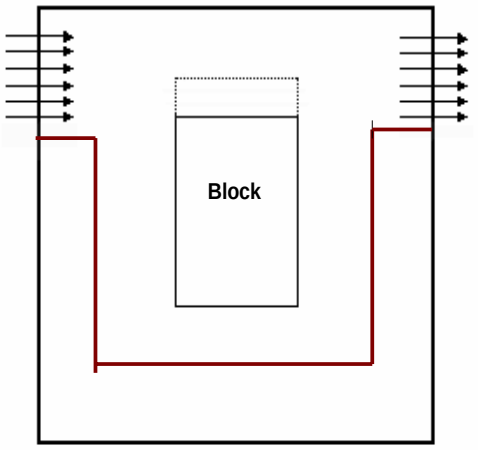

Fig. 8 Cartoon of the set-up for irrotational incompressible flow.

and the continuity equation reduces to:

$$\nabla \cdot \bar{V} = \frac{\partial U}{\partial x} + \frac{\partial V}{\partial y} = 0 \qquad \text{or} \qquad \mathbf{\partial^2 / \partial x^2 + \partial^2 / \partial y^2 = 0}$$

Fig. 8 illustrates a cartoon of the set-up for a numerical solution for irrotational incompressible flow. The numerical solution of Laplace's equation for this problem requires that the integral $\frac{\partial \phi}{\partial n} = 0$ (where n is the normal to the boundary). Thus in Fig. 8 one sets the Φ-field to the match the desired input and output along the external edges of the grid. Of course, all the boundary points on the block inside the grid are zero and there are no calculations in the block. The initial conditions within the grid are set with Φ = 0. A standard numerical method for Laplace's equations provides the solution for Φ within the interior of the grid. From this Φ-field, *U* and *V* can be calculated from the definition of Φ above.

The solution of Laplace's equation for this case of partial blocking of the flow by a raised surface (the extended block in Fig. 8, though the height is not to scale) yields South channel flow of 28.2 % of (South flow **plus** North flow) and 19.4 % of the input flow. The height selected in the calculation corresponds to that used for the full equations for compressible flow.

4.2 Compressible Flow Theory

Simulating the partial flow in the UCAR air sampler with compressible flow theory requires prognostic equations for *ρ , T, U, and V.* Using the continuity equation, the momentum equations, the energy equation, the equation of state $(P = \rho RT)$ and assuming a calorically perfect gas $(e = C_V T)$ the set of four prognostic nonlinear equations for *ρ, T, U, and V* can be closed and are listed below. No prognostic equation is required for pressure P since density and temperature are predicted and P = ρRT.

$$\frac{\partial \rho}{\partial t} = -U\frac{\partial \rho}{\partial x} - V\frac{\partial \rho}{\partial y} - \rho\left(\frac{\partial U}{\partial x} + \frac{\partial V}{\partial y}\right) \tag{3}$$

$$\frac{\partial U}{\partial t} = -U\frac{\partial U}{\partial x} - V\frac{\partial U}{\partial y} - \frac{1}{\rho}\frac{\partial P}{\partial x} \tag{4}$$

$$\frac{\partial V}{\partial t} = -U\frac{\partial V}{\partial x} - V\frac{\partial V}{\partial y} - \frac{1}{\rho}\frac{\partial P}{\partial y} \tag{5}$$

$$\frac{\partial T}{\partial t} = -U\frac{\partial T}{\partial x} - V\frac{\partial T}{\partial y} - \frac{P}{C_V \rho}\left(\frac{\partial U}{\partial x} + \frac{\partial V}{\partial y}\right) \tag{6}$$

Using $P=\rho RT$, $\quad \frac{\partial P}{\partial x} = R\left(\rho\frac{\partial T}{\partial x} + T\frac{\partial \rho}{\partial x}\right) \qquad \frac{\partial P}{\partial y} = R\left(\rho\frac{\partial T}{\partial y} + T\frac{\partial \rho}{\partial y}\right)$

and nondimensional variables (defined with a prime ') $\quad T' = \frac{T}{T_0} \qquad \rho' = \frac{\rho}{\rho_0}$

$$x' = \frac{x}{L} \qquad y' = \frac{y}{L} \qquad t' = \frac{t}{L/a_0}$$

$$a_0 = \sqrt{\gamma R T_0} \qquad U' = \frac{U}{a_0} \qquad V' = \frac{V}{a_0}$$

The equations reduce to those below (written without the primes):

$$\frac{\partial \rho}{\partial t} = -U\frac{\partial P}{\partial x} - V\frac{\partial \rho}{\partial y} - \rho\left(\frac{\partial V}{\partial x} + \frac{\partial V}{\partial y}\right) \tag{7}$$

$$\frac{\partial U}{\partial t} = -U\frac{\partial U}{\partial x} - V\frac{\partial U}{\partial y} - \frac{1}{\gamma}\left(\frac{\partial T}{\partial x} + \frac{T}{\rho}\frac{\partial \rho}{\partial x}\right) \tag{8}$$

$$\frac{\partial V}{\partial t} = -U\frac{\partial V}{\partial x} - V\frac{\partial v}{\partial y} - \frac{1}{\gamma}\left(\frac{\partial T}{\partial y} + \frac{T}{\rho}\frac{\partial \rho}{\partial y}\right) \tag{9}$$

$$\frac{\partial T}{\partial t} = -U\frac{\partial T}{\partial x} - V\frac{\partial T}{\partial y} - (\gamma - 1)T\left(\frac{\partial U}{\partial x} + \frac{\partial V}{\partial y}\right) \tag{10}$$

Fig. 9 shows a set-up for simulating this problem. We begin the simulation with the flow already accelerated by the convergent nozzle design described in section 3. The input (*I*) area between rows ***IJ1*** **to** ***IJ2*** on the top left of Fig. 9 represents the flow at the throat. Note that the area of the nozzle from the throat to the exit is constant with ***IJ1*** = ***KJ1*** **and** ***IJ2*** = ***KJ2*****.** The width of the flow can be controlled by changing the columns and rows through the I and J variables **(IJ1, ILE, IRW, and JLN, JRN).** The flow can be controlled by raising or lowering the height of Block 1 in the diagram **(*J1N*).** The index **I** varies in the x-direction from 1-241, and **J** in the y-direction from 1-241

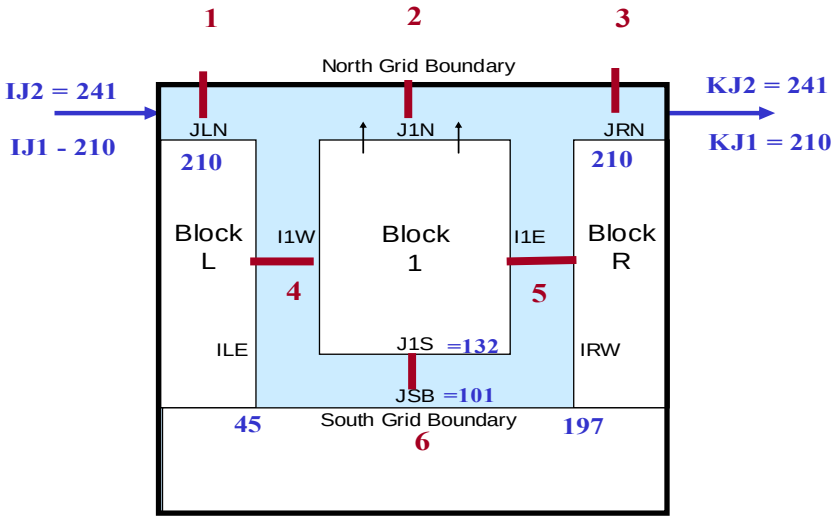

Fig. 9. Simulation set-up. Check points in red with coordinates given in text

This simulation uses a fixed rectangular grid, 2nd order accuracy for spatial finite differencing, 4th order Runge Kutta time differencing, and an artificial viscosity to help control unsteady compression and expansion waves. The initial conditions for the

nondimensional mass variables are $\rho = 1$, T=1, $P = \rho * T = 1$ (in nondimensional form), and the velocity values are U=V=0 in the grid interior. A steady inflow of U=0.72 is input at the source region of Fig. 9 (between rows IJ1 and IJ2) and time integration evolves the flow through the north, south, east, west channels, and exit.

One would be prudent to check the complex code, with the boundary assumptions and numerical techniques that have been used, to see if the code is correct and stable. A perfect flow condition to check is the case shown at the top of Fig. 10.

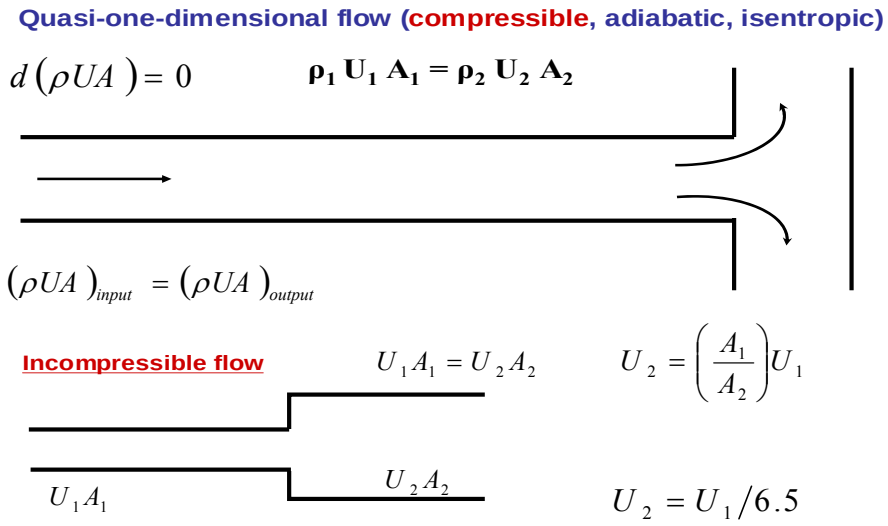

Fig. 10. Example of compressible flow (top) and incompressible flow (bottom)

The simulation of a strong compression wave is created as follows. The same grid of 241 x 241 points is used **with a subset of points used to create a flow of Mach = 0.72 down the center of the grid from west to east (as shown at the top of Fig. 10).** The width of the horizontal flow from west to east is 15 grid units. The two outflow regions to the north and south are 8 grid units each. The initial conditions are U(I,J) = V(I,J) = 0 at all the points – except at the entrance where the initial input rows have

U(1,J) = 0.72 (a flow of Mach = 0.72) for **J = 114 to J = 128**. The initial values for density (ρ), temperature (T) and pressure (P) are all set equal to 1.0 for all grid points. The flow and all variables are held constant at the entrance. The exit values are predicted as a function of time ("floated") but the exit pressure **(P_E)** must be specified (Anderson,1995). Thus, the method of achieving this is to predict T at the **north and south** exit points **[T(I,N) and T(I,1)]** by linearly extrapolating from the values at the interior points:

T(I, N) = 2.0 T(I, N-1) – T(I, N-2)	T(I , 1) = 2.0 T(I , 2) – T(I , 3)
ρ(I, N) = P_E / T(I, N)	ρ(I, 1) = P_E / T(I, 1) **P_E = 1.0**
U(I, N) = 2.0 U(I, N-1) – U(I, N-2)	U(I, 1) = 2.0 U(I, 2) – U(I, 3)
V(I, N) = 2.0 V(I, N-1) – V(I, N-2)	V(I, 1) = 2.0 V(I, 2) – V(I, 3)
P(I, N) = ρ (I, N) T(I, N)	P(I ,1) = ρ (I, 1) T(I, 1)

Thus we see that pressure is always specified (constant) at the two exits (N and S).

The see from the top of Fig. 10 that the mass flux times the area input (I) must equal the flux times the area exit (E) or: $\rho_I U_I A_I = \rho_E U_E A_E$.

In this case the exit velocities are V(I, N) with V positive toward the north and V(I ,1) with V negative toward the south.

The simulation of the surge of mass flux down the center channel is remarkably accurate and stable. Fig. 11 indicates the evolution of the RATIO = flux output / flux input, which means the average flux out of the 16 columns (8 to the north and 8 to the south) compared to the 15 rows of average flux input. One sees that the surge finally reaches the exits after 970 iterations, surpasses the initial mass flux by about 20%, and then settles down toward the steady state of mass balance. The mass flux is extremely

nonlinear throughout the channel – with a build up of mass at the end of the channel at the east wall. The grid variables are entirely symmetric on each side of the center line of the channel **(row J = 121).** For example, the V-components of velocity at corresponding grid points away from the center line have exactly the same magnitude (though with a positive sign for points north of the center line and a negative sign for points south of the center line). Thus, the numerical results of this "tee flow" were very acceptable.

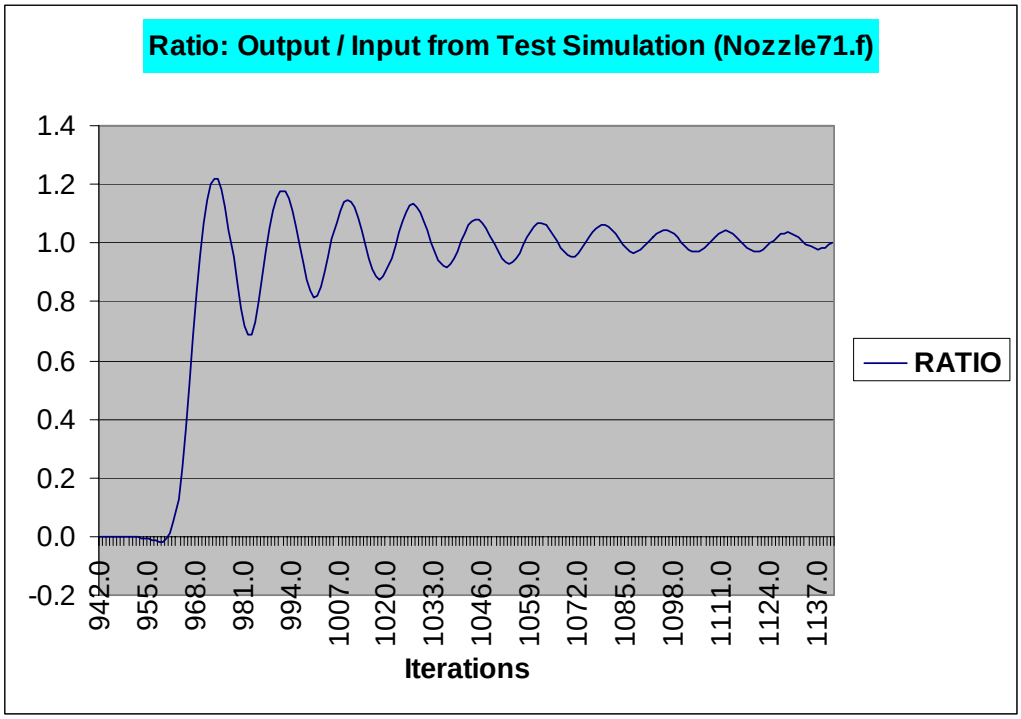

Fig. 11. Mass flux ratio (output / input) results for the test "T –shaped" channel

Returning to the flow in the channels shown in Fig. 9, which is intended to simulate the conditions within the air sampler and hoses of the WVSS-II, we use the same initial surge conditions as for the test case ("T-channel" flow), but now we have all channels with a width of 32 grid points. Thus, the (I, J) values are indicated in **blue** in

Fig. 9 along with six **red** check points: **#1 (24,J), #2 (124,J), #3 (224,J), #4 (I,156), #5 (I,156), #6 (124,J)**, and of course at the **exit (241, J)** where J = 210 to 241.

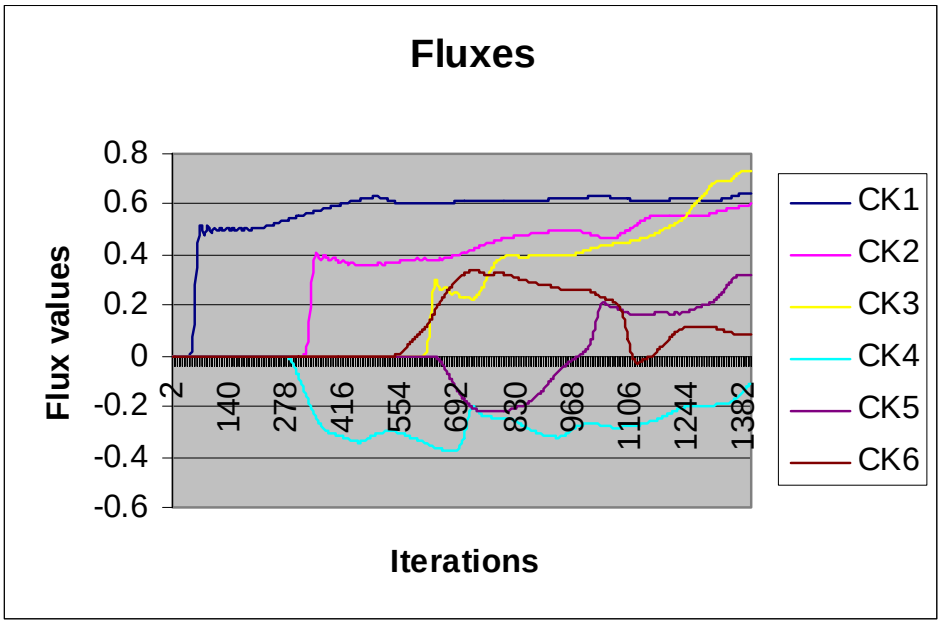

Fig. 12. Fluxes (density x velocity) at various check points (see text)

This is a complex flow regime shown in Fig.12 where the mass fluxes at various check points are shown. Small amplitude compression waves follow the surge. The surge reaches check points CK1, CK2 and CK3 at 70,346, and 662 iterations respectively. Flow into the west channel is of course negative (southward). There is a vortex created in the west channel as the surge flow passes the corner heading south. This becomes a substantial vortex covering about 20% of the channel. A better result occurs when the equations are cast in conservative form (Anderson, 1995). The amplitude of the vortex is about $1/4^{th}$ the area and 1/2 the amplitude with the new equations. An example of the vortex produced by flow over a forward facing corner in shown in Fig. 13 from Anderson (1995) – though the figure should be rotated 90 degrees to match the corner in question.

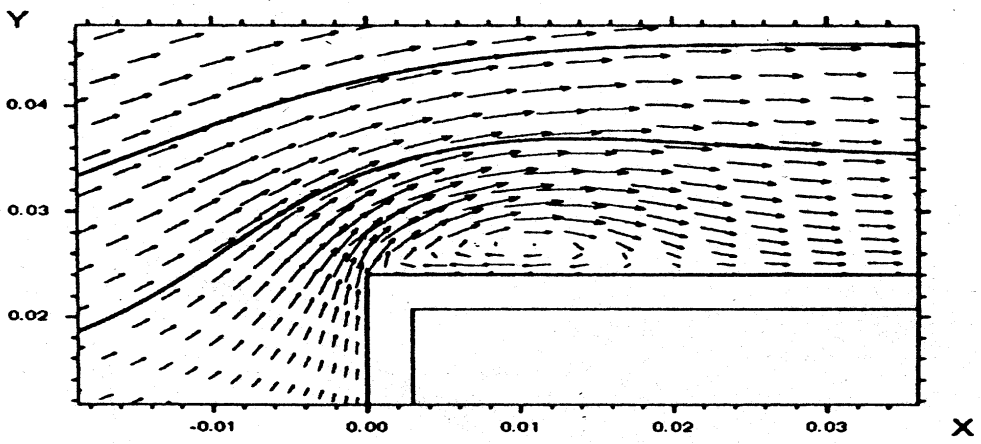

Figure 13. Compressible subsonic flow over a forward facing step.

The flow in the north channel eventually reaches the east channel and turns southward. This flow will eventually collide with the flow coming from the west in the south channel. Eventually this flow reverses as seen in the flux diagram of Fig.12. (CK5).

The flow eventually becomes reasonably balanced and the compression waves exiting the system become damped and the flow reaches the desired ratio of flux output divided by flux input reaching the ratio value of one as seen in Fig. 14. [The results in these figures are for the condition $\Delta J = 3$.]

The actual time required for this "near steady state" is determined as follows. Since $t' = t / (L / a_0)$ and $a_o = 316$ ms^{-1}, one can use $L = 13.65$ cm; thus, $L / a_o = 4.32 \times 10^{-4}$ seconds. The nondimensional time required to achieve the ratio = 1 for the case $\Delta J = 3$ was 4.941 (for the 1402 iterations). **Thus, the actual time required to come to near**

steady state was (4.32×10^{-4}) (4.941) = 2.13×10^{-3} seconds or approximately 2.1 milliseconds.

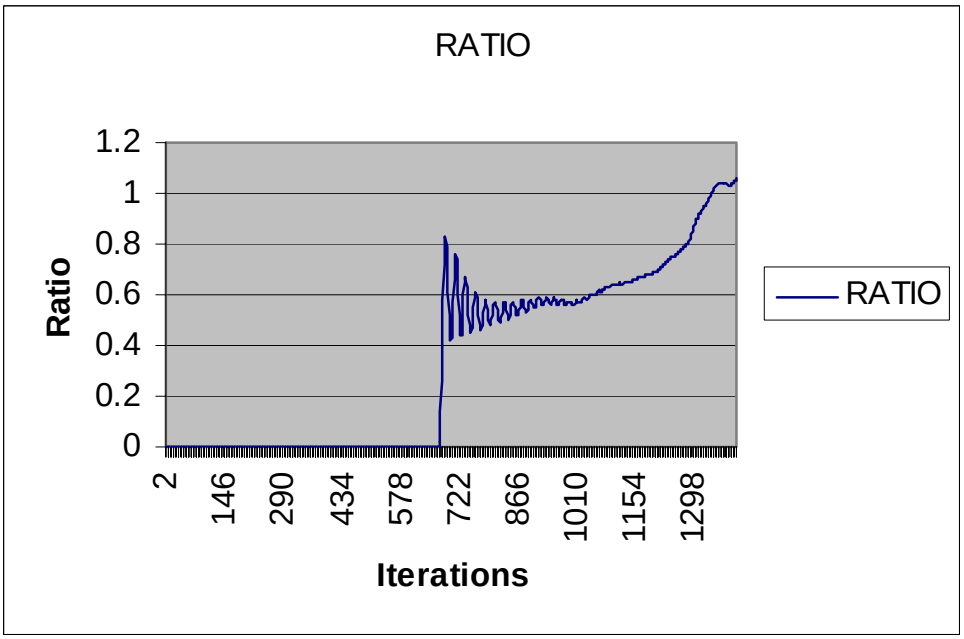

Figure 14. Ratio of flux output divided by the flux input

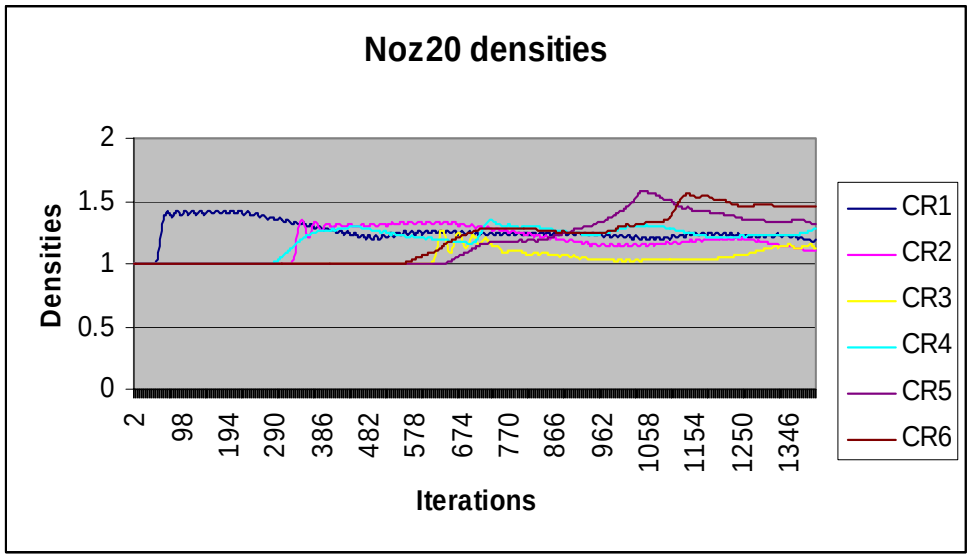

Figure 15. Densities at the various check points

The densities at the various check point are shown in Fig. 15. One can clearly discern when the surge passes the check points as the initial non-dimensional densities rapidly raise from unity. Only after the flow has finished sloshing back and forth do the densities become relatively close – even then the mass build–up in the south channel (from two flows initially moving toward each other) is still dissipating.

Table 1 indicates the summary of the calculations. There are 32 rows of input and the height of Block 1 (J1N) is varied from $\Delta J = 0$ (which is level with the input field) to ΔJ=6. The table shows the flow (in terms of Mach number) in the North channel, the South channel, and the percent of the South channel flow to the **input** flow for various values of ΔJ.

In preparing Table 1 the flow values used were those calculated values when the mass flux (density times velocity) of the **input** matched the mass flux at the **exit** (where all variables were floated and thus changed over time). For this problem (as seen in the top of Fig. 10) the mass flux is conserved:

$$(\rho)(U)(area)_{input} = (\rho)(U)(area)_{output}$$

Note that the South channel has the same width, thus the same cross-section area, as the **input** and **output** areas. However, the North channel cross-section area changes with increased height of the flow obstacle -- increasing the relative flow in the north – at the expense of the flow in the south. Our only interest is in the percentage of the total input flow to that flow which passes through the south channel. This is shown in the final column of Table 1. The equations were in conservative form and were successful in limiting the effect of compression and expansion waves from reflecting off the downstream boundary. They were quite representative with lab results as shown below.

Table 1 – Simulated flows (U component) in the North and South Channels

ΔJ	Flow North Channel	Flow South Channel	% Flow in South Channel to Initial Flow
0	0.5173	0.0273	3.8
1	0.5370	0.0392	5.5
2	0.5396	0.0433	6.1
3	0.5589	0.0559	7.9
4	0.5579	0.0608	8.6
5	0.5688	0.0728	10.3
6	0.5510	0.0762	10.7

Using $\Delta J = 3$ in Table 1 produces an average flow in the South channel of (224.4)(0.079) = 17.7 ms^{-1}. The modified flow through the "South channel" represents the flow through the hose to the measurement cell.

At this stage, the flow is slow enough in the hose to be considered incompressible and we can use the information contained in the **bottom of Fig. 10**. Here the flow in the measurement cell (U_2) in the cell area (A_2) is given by : $U_2 = U_1 / 2.6$ since the area ratio A_1 / A_2 has been designed to be 1 / 2.6. Thus the velocity in the measurement cell for this case at 20,000 feet for a standard atmosphere is 17.7 / 2.6 = 6.81 = 6.8 m/s.

The flow exiting the hose would be the ratio of the inner hose diameter to the hole diameter in the bottom of the air sampler (.375 /.25 = 1.5. Thus the flow exiting the hose would be 7.9 % / 1.5 = 5.3 %. A slower laboratory flow input showed that 8 % of the input flow exited the hose. **The simulations indicate that a higher percentage of flow occurs when the input flow in slower.** Input of M = 0.355 (one half of that used in the simulations) provides a Table 1 value of 12.3 – implying 8.2% would exit the hose.

5. Efficiency of the Particle Removal

The issue of removal of particles (aerosols or ice crystals) within the air sampler in the cold, upper troposphere is related to the subject of flow of complex mixtures in pipes (cf. Gover and Aziz, 1972). The total system continuity equation for a two-phase system with ρ_α the density of the less dense phase (water vapor) and ρ_β the denser phase (aerosols or ice crystals) is:

$$\frac{d}{dt}\left(\int_{\mathcal{V}_\alpha}\rho_\alpha d\mathcal{V}+\int_{\mathcal{V}_\beta}\rho_\beta d\mathcal{V}\right)=-\int_{A_{e\alpha}}\rho_\alpha \mathbf{v}_\alpha\cdot d\mathbf{A}-\int_{A_{e\beta}}\rho_\beta \mathbf{v}_\beta\cdot d\mathbf{A}$$

Where $\mathcal{V}$ = volume, **v** = velocity vector, and **A** = area. The mass flow rates of the individual phases at the inlet or the outlet of the pipe are given by equations such as

$$M_{\alpha 1}=\int_{A_{\alpha 1}}\rho_\alpha \mathbf{v}_\alpha\cdot d\mathbf{A}$$

for the α phase at the inlet (subscript = 1 for inlet and = 2 for outlet). For one-dimensional flow parallel to the *x*-axis one would have

$$M_{\alpha 1}=\rho_{\alpha 1}V_{\alpha 1}E_{\alpha 1}A=\text{ rate of mass influx of the }\alpha\text{ phase} \tag{11a}$$

$$M_{\beta 1}=\rho_{\beta 1}V_{\beta 1}E_{\beta 1}A=\text{ rate of mass influx of the }\beta\text{ phase} \tag{11b}$$

$$M_{\alpha 2}=\rho_{\alpha 2}V_{\alpha 2}E_{\alpha 2}A=\text{ rate of mass efflux of the }\alpha\text{ phase} \tag{11c}$$

$$M_{\beta 2}=\rho_{\beta 2}V_{\beta 2}E_{\beta 2}A=\text{ rate of mass efflux of the }\beta\text{ phase} \tag{11d}$$

where V_α and V_β are the cross-sectional area average velocities, E_α is the average volume fraction of the α phase over a differential length of pipe and therefore is the fractional cross-sectional area occupied by the α phase, i.e,

$$E_\alpha=\frac{A_\alpha}{A}\quad\text{and}\quad E_\alpha+E_\beta=1$$

In the special case where the inflows $M_{\alpha 1}$ and $M_{\beta 1}$ are constant with time and where the flow in the pipe is stabilized, resulting in a constant mass in the pipe, the continuity equation reduces to the following:

$$M_{\alpha 1} + M_{\beta 1} = M_{\alpha N} + M_{\alpha S} + M_{\beta N} + M_{\beta S} = M_{\alpha 2} + M_{\beta 2}$$

where the subscripts N and S refer to variables in the North and South channels respectively. One does not have enough information to solve this equation without equipment to measure aerosol density inputs and outputs. However, our real interest is in the efficiency of particle removal or the ratio:

$$R = M_{\beta N} \Big/ M_{\beta N} + M_{\beta S}$$

in the stable steady state. This ratio can be simplified by the quite good assumption that $V_\alpha = V_\beta$; that is, the aerosols move with the same speed as the flow which is the fundamental assumption used in Doppler lidar wind measurement systems and valid for all but the largest of aerosol particles, which are quite few. The ratio then reduces to:

$$R = \frac{\rho_\beta U_N E_{\beta N} A_N}{\rho_\beta U_N E_{\beta N} A_N + \rho_\beta U_S E_{\beta S} A_s}$$

dividing all terms by the numerator

$$R = \frac{1}{1 + \left(\frac{A_S}{A_N}\right)\left(\frac{U_S}{U_N}\right)\left(\frac{E_{\beta S}}{E_{\beta N}}\right)} \qquad (12)$$

The first ratio in the denominator is known before the computation starts and is given by ΔJ in Table 1. This area ratio is given by:

$$A_S / A_N = (\Pi\, d^2 / 4) / (\Pi)\, [\, (32 - \Delta J)\, (\, d / 32)\,]^2 / 4$$

$$= [\, (32) / (32 - \Delta J)\,]^2 = (32 / 29)^2 = 1.218 \qquad \textbf{with } \Delta J = 3$$

The second ratio in the denominator comes from the results of our simulations for the case with ΔJ = 3. Here one has $U_S / U_N = (0.0559) /(0.5589) = 0.1000$

Assuming for the moment that the third ratio $\left(E_{\beta S} / E_{\beta N}\right) = 1$ we have from Eq. 12

R = 1 / [1 + (1.218) (0.100)] = 0.891 = 89.1 %.

The third ratio $\left(E_{\beta S} / E_{\beta N}\right)$ in the denominator of Eq. (12) is a bit more complicated. Knowing the initial aerosol average volume fractions (the *E* values), one could integrate the existing Navier-Stokes equations defined above and come up with an estimate of this third ratio. Not having this capability, one can provide a qualitative argument for the range of this ratio. This is presented below along with the estimated impact on the efficiency of particle removal by the air sampler.

One extreme value for this ratio is 1, which was already used above to give a lower limit of **89 %** as the efficiency of the air sampler to remove particles. This ratio of $\left(E_{\beta S} / E_{\beta N}\right) = 1$ states that the steady state fractional volume of particles is the same in both the South and North channels. This is **extreme** because the momentum of the heavier particles leaving the entrance in the accelerated flow stream shown in Fig. 7 would surely carry most of them directly over the aperture leading to the measurement cell (down the North channel).. Thus, the ratio $\left(E_{\beta S} / E_{\beta N}\right)$ is certainly less than 1.

It would also be extreme to suggest that this ratio is **zero—all** the particles being passed over this aperture. A lower limit for $\left(E_{\beta S} / E_{\beta N}\right)$ [which must lie between 0 and 1] is suggested below, which will provide an **upper** limit on efficiency.

The density of the particles themselves is assumed constant in either channel. One could use the air mass flux values from the simulations used to produce Table 1. The

mass flux calculations for each of the channel **check points (CK6 and CK2 for the South and North channels respectively)** produced the ratio of flux in the South divided by flux in the South channel of: South/North = 0.131. This seems a bit optimistic – that the particles follow the distribution of the moist atmospheric mass. This would give an optimistic upper limit for the ultimate ratio we are after of :

R = 1 / [1 + (1.218) (0.100) (0.131)] = 0.984 = 98.4 %

However, one can be more conservative and assume that the heavier particle distribution is approximated by the solution of Laplace's equation. Using our previous solution of this equation for a similar obstacle height (see Section 4) one would have $\left(E_{\beta S} / E_{\beta N}\right)$ = 0.282. In this case, one has the ratio:

R = 1 / [1 + (1.218) (0.100) (0.282)] = 0.967 = 96.7 %

Thus, the range of efficiency of the particles removed by the UCAR air sampler is estimated to be **89 to 97 %** of whatever fraction of particles is encountered.

6. Application of the mobile air sampler

6.1 Composite Upper Air Observing System for Weather and Climate

Satellite remote sensing of the key atmospheric parameters in the lower troposphere is quite poor and is likely to remain that way for the foreseeable future with regard to vertical resolution and accuracy for winds and water vapor. This leaves the atmospheric science community involved with weather and climate being dependent upon the national radiosonde system or expensive research aircraft for operations and research. The radiosonde system coverage is shown with the blue dots of Fig. 16. This gives vertical profiles of winds, temperature, and water vapor twice per day at approximately 350 km horizontal coverage over the continental United States (CONUS). This space/time coverage is synoptic scale – not the mesoscale (smaller scale depiction of

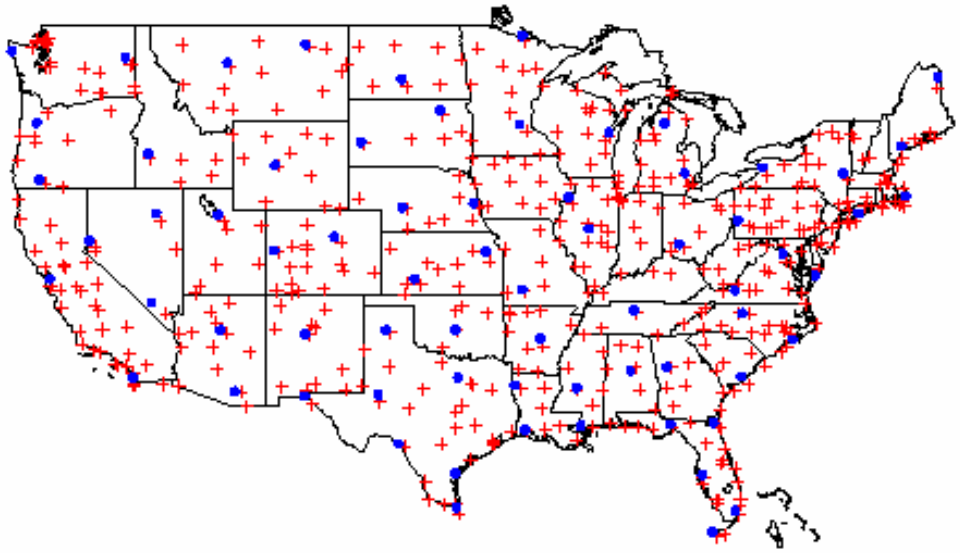

Fig. 16. Continental United States area with blue dots showing locations of existing radiosonde balloon release sites and red "plus" signs showing airports routinely used by major and regional air carriers.

features in space/time) required for aviation weather, proper prediction of precipitation, more accurate storm warnings, etc. Moreover, the accuracy of radiosondes with respect to water vapor has always been questioned under certain conditions, e.g., Wade (1994), Wade, et al (1993), Miloshevich, et al. (1998).

A plan to break this "synoptic scale barrier" to upper air measurements has been put forward. Using commercial aircraft equipped with the WVSS-II, it is possible to provide winds, temperature, and water vapor profiles at a rate of approximately 100 times the frequency per day of the radiosonde system. Fig 16 shows the CONUS airports used by major and regional air carriers (red "plus signs" in the Fig.). The major air carriers average 4 ascents and 4 descents per day per aircraft. The author has an analysis that leads to the average cost per commercial aircraft profile being less than $1.50 each – this for winds, temperature, and water vapor. The recurring cost of a radiosonde profile is approximately $250.00 each today and going to much higher costs when they become Global Positioning System (GPS) sondes.

The aircraft coverage is not uniform in time – the void in passenger travel from midnight to six a.m. is only partially filled by the peak travel of the package carriers during these hours. Nevertheless, the commercial aircraft measurement system is a perfect compliment to the existing satellite system and helps bring upper atmospheric science into the mesoscale regime for the first time. The National weather Service of the United States has started a program to provide the WVSS-II water vapor system for up to 1600 commercial aircraft.

6.2 Mesoscale Upper Air Atmospheric Chemistry

Atmospheric chemistry has primarily been conducted by in-situ surface measurements, flask sampling of air at the surface, vertical profiling via balloon launches in research projects and/or field campaigns, many research aircraft flights with sophisticated instruments, special efforts to gather species information in a delayed mode from flight level data from a few transoceanic commercial aircraft flights, and remote sensing from various satellites. Except for an ozone sonde network, no systematic upper air observing system for atmospheric chemistry has been implemented for a variety of reasons (financial and otherwise).

The diode laser chosen for water vapor can be replaced with different diode lasers chosen for a few chemical species. The same hardware for the WVSS-II can be used for the species application with quantum cascade (QC) lasers (see Fig. 2). The new QC lasers are being used in many research facilities around the world. The QC lasers are just beginning to emerge commercially but they have several advantages (cf. Capasso, et al, 2002), some of which are described below. The small diode laser would be replaced by the even smaller QC laser to match the species. A different light detector would be required and would fit within the space is the existing System Electronics Box.

QC lasers are fabricated by molecular beam epitaxy, a crystal growth technique capable of depositing thin films (layers a few atoms thick) of alloy material such as aluminum (Al), gallium (Ga), arsenide (As), and indium (In). It is the suitably designed thickness of the layers that determines the emission wavelength of interest – rather than the choice of material used in the fabrication. In QC lasers the electron is recycled into adjacent active regions giving rise to a cascading emission of photons – resulting in very

high power for such a small device (typically 5-20 μm wide and 1-3 mm long). The QC lasers have high reliability, low failure rates, and long lifetimes.

The most valuable aspect of QC lasers is the fact that they can emit laser energy above the near infrared (IR) range of diode lasers and have been proven to work over the mid-IR range of 4-24 μm. This range is then capable of detecting a host of chemical species that are important to air quality in the short-term and global change in the long-term; e.g., ozone (O_3), carbon monoxide (CO), methane (CH_4), nitric oxide (NO), etc.

The use of such QC lasers with the UCAR air sampler and May's (1998) derivative spectroscopy techniques on commercial aircraft could supply the same kind of mesoscale coverage for various chemical species as implied in Section 6.1 for water vapor profiles. **The best approach** is to time share two lasers mounted on the same plane within a single measurement cell. One could imagine water vapor and three other chemical species measured from the same commercial aircraft in such a configuration This would produce real-time species profiles.

The costs of a QC laser system are still rather expensive. Species profiles would be an order of magnitude higher than those for water vapor only. However, the profiles would include time, latitude, longitude, winds, temperature, water vapor mixing ratio, and three mixing ratios for the three chemical species at each point in the profile. Today, such vertical resolution for water vapor is every 6 seconds (approximately 100 meters) with every 3 seconds an option (50 meters). Such real-time chemical species profiles would usher in the age of mesoscale atmospheric chemistry.

References

Anderson, J.D., Jr., 1995: *Computational Fluid Dynamics*, McGraw-Hill, New York, 547

Anderson, J. D., Jr., 2003: *Modern Compressible Flow*, Third Edition, McGraw-Hill, New York, 760p.

Bates, J. J., X. Wu, and D. L. Jackson, 1996: Interannual variability of upper-troposphere water vapor band brightness temperature. *Journal of Climate*, **9**, 427–438.

Capasso, F., C. Gmachl, P. L. Sivco, and A. Y. Cho, 2002: Quantum cascade lasers. *Physics Today*, May, 2002, 34–40.

Crook, N. A., 1996: Sensitivity of moist convection forced by boundary layer processes to low-level thermodynamic fields. *Mon. Wea. Rev.*, **124**, 1767–1785.

Emanuel, K. and coauthors, 1995: Report of the first prospectus development team of the US Weather Research Program to NOAA and the NSF. *Bull. Amer. Meteor. Soc.*, **76**, 1194–1208.

Fleming, R. J., 1996: The use of commercial aircraft as platforms for environmental measurements. *Bull. Amer. Meteor. Soc.,* **77**, 2229-2242.

Fleming, R. J., D. R. Gallant, W. Feltz, J. G. Meitin, W. R. Moninger, S. F. Williams, and R. T. Baker, 2002: Water vapor profiles from commercial aircraft. FAA Report, January 10, 2002, 37p. Available at: http://www.joss.ucar.edu/wvss/.

Gover, G. W. and K. Aziz, 1972: *The Flow of Complex Mixtures in Pipes*, Van Nostrand Reinhold, New York, 792p.

Lorenc, A. C., D. Barker, R. S. Bell, B. Macpherson, and A. J. Maycock, 1996: On the use of radiosonde humidity observations in mid-latitude NWP. *Meteorol. Atmos. Phys.*, **60**, 3–17.

May, R. D., 1998: Open-path, near-infrared tunable diode laser spectrometer for atmospheric measurements of H_2O. *Journal of Geophysical Research*, **103**, 19,161–19,172.

May, R. D. and C. R. Webster, 1993: Data processing and calibration for tunable diode laser harmonic absorption spectrometers. *J. Quant. Spectrosc. Radiat. Transfer.* **49**, 335–347.

Melfi, S. H., D. Whiteman, and R. Ferrare, 1989: Observations of atmospheric fronts using Raman lidar moisture measurements. *J. App. Meteor.* **28**, 789–806.

Miloshevich, L. M., A. J. Heymsfield, and S. J. Oltmans, 1998: Undermeasurement of high relative humidities in the upper troposphere by Vaisala RS80-A radiosondes. Preprints, *Tenth Symp. on Meteorological Observations & Instrumentation*, Phoenix, AZ, Amer. Meteor. Soc., 74–79.

Wade, C. G., 1994: An evaluation of problems affecting measurements of low relative humidity on United States radiosonde. *J. Atm. And Oceanic Tech.*, **11**, 687-700.

Wade, C. G. and B. Schwartz, 1993: Radiosonde humidity observations near saturation. Preprints, *Eighth Symp. on Meteorological Observations and Instrumentation*, Anaheim, CA, Amer. Meteor. Soc., 44–49.

Warneck, P, 1988: Chemistry of the Natural Atmosphere, Academic Press, San Diego, 757 p.

Appendix

The total temperature (T_0) measured within the probe of an aircraft moving at Mach number (M) is given by:

$$\frac{T_0}{T} = 1 + \frac{\gamma - 1}{2} M^2 \tag{A1}$$

where $\gamma = 1.4$.

The relationship between total pressure (P_0) and static pressure (P) is given by:

$$\frac{P_0}{P} = \left(1 + \frac{\gamma - 1}{2} M^2\right)^{\gamma/(\gamma-1)} \tag{A2}$$

A third relation completing the set is that for total density (ρ_0) and static density (ρ) given by:

$$\frac{\rho_0}{\rho} = \left(1 + \frac{\gamma - 1}{2} M^2\right)^{1/(\gamma-1)} \tag{A3}$$